

Diagnosing the sensitivity of grounding line flux to changes in sub-ice shelf melting

Tong Zhang¹, Stephen F. Price¹, Matthew J. Hoffman¹, Mauro Perego², and Xylar Asay-Davis¹

¹Fluid Dynamics and Solid Mechanics Group, Los Alamos National Laboratory, Los Alamos, NM, 87545, USA

²Center for Computing Research, Sandia National Laboratories, Albuquerque, NM, 87185, USA

Correspondence: T. Zhang (tzhang@lanl.gov), S. Price (sprice@lanl.gov)

Abstract. Using a numerical ice flow model, we study changes in ice shelf buttressing and grounding line flux due to localized ice thickness perturbations, a proxy for localized changes in sub-ice shelf melting. From our experiments, applied to idealized (MISMIP+) and realistic (Larsen C) ice shelf domains, we identify a correlation between a locally derived buttressing number on the ice shelf, based on the first principal stress, and changes in the integrated grounding line flux. The origin of this correlation, however, remains elusive from the perspective of a theoretical or physically-based understanding. This and the fact the correlation is generally much poorer when applied to realistic ice shelf domains motivates us to seek an alternative approach for predicting changes in grounding line flux. We therefore propose an adjoint-based method for calculating the sensitivity of the integrated grounding line flux to local changes in ice shelf geometry. We show that the adjoint-based sensitivity is identical to that deduced from pointwise, diagnostic model perturbation experiments. Based on its much wider applicability and the significant computational savings, we propose that the adjoint-based method is ideally suited for assessing grounding line flux sensitivity to changes in sub-ice shelf melting.

1 Introduction

Marine ice sheets like that overlying West Antarctica (and to a lesser extent, portions of East Antarctica) are grounded below sea level and their bedrock would remain so even after full isostatic rebound (Bamber et al., 2009). This and the fact that ice sheets generally thicken inland leads to a geometric configuration prone to instability; a small increase in flux at the grounding line thins the ice there, leading to floatation, a retreat of the grounding line into deeper water, further increases in flux (due to still thicker ice), and further thinning and grounding line retreat. This theoretical “marine ice sheet instability” (MISI) mechanism (Mercer, 1978; Schoof, 2007) is supported by idealized (e.g., Schoof, 2007; Cornford et al., 2020) and realistic (e.g., Cornford et al., 2015; Royston and Gudmundsson, 2016) ice sheet modeling experiments, and some studies (Joughin et al., 2014; Rignot et al., 2014) argue that such an instability is currently under way for outlet glaciers of Antarctica’s Amundsen Sea Embayment. The relevant perturbation for grounding line retreat in the Amundsen Sea Embayment is thought to be intrusions of relatively warm, intermediate-depth ocean waters onto the continental shelves, which have reduced the thickness and extent of marginal ice shelves via increased sub-ice shelf melting (e.g., Jenkins et al., 2016). These reductions are important because fringing ice shelves restrain the flux of ice across their grounding lines farther upstream – the so-called “buttressing” effect of ice shelves

25 (Gudmundsson et al., 2012; Gudmundsson, 2013; De Rydt et al., 2015; Haseloff and Sergienko, 2018; Pegler, 2018a, b) –
which makes them a critical control on the rate of ice flux across Antarctic grounding lines into the ocean.

On ice shelves, the driving stress (from ice thickness gradients) is balanced by gradients in membrane stresses (Hutter, 1983; Morland, 1987; Schoof, 2007). For an ice shelf in one horizontal dimension (x, z), these longitudinal stress gradients provide no buttressing (Schoof, 2007; Gudmundsson, 2013). For realistic, three-dimensional ice shelves, however, buttressing results
30 from three main sources: 1) along-flow compression, 2) lateral shear, and 3) “hoop” stress (Wearing, 2016). Compressive and lateral shear stresses can provide resistance to extensional ice shelf flow through along- and across-flow stress gradients. The less commonly discussed “hoop” stress is a transverse stress arising from azimuthal extension in regions of diverging flow (Pegler and Worster, 2012; Wearing, 2016). Due to the complex geometries, kinematics, and dynamics of real ice shelves, an understanding of the specific processes and locations that control ice shelf buttressing is far from straightforward.

35 Several recent studies apply whole-Antarctic ice sheet models, optimized to present-day observations, towards improving our understanding of how Antarctic ice shelves impact ice dynamics farther upstream or limit flux across the grounding line. Fürst et al. (2016) proposed a locally derived “buttressing number” (extended from Gudmundsson, 2013) for Antarctic ice shelves and used it to guide the location of calving experiments whereby the removal of progressively larger portions of the shelves near the calving front identified dynamically “passive” shelf regions; removal of these regions (e.g., via calving) was
40 found to have little impact on ice shelf dynamics or the flux of ice from ice upstream to the calving front. Reese et al. (2018) conducted a set of diagnostic, forward-model, perturbation experiments to link small, localized decreases in ice shelf thickness to changes in integrated grounding line flux (GLF), thereby providing a map of GLF sensitivity to local increases in sub-ice shelf melting.

Motivated by these studies, we build on and extend the methods and analysis of Fürst et al. (2016) and Reese et al. (2018)
45 to address the following questions: (1) How do changes in ice-flux across the grounding line relate to local estimates of ice-shelf buttressing evaluated on the ice shelf? (2) What are the limitations of locally derived buttressing metrics when used to assess GLF sensitivity? (3) Can new methods overcome these limitations? Our specific goal is to identify robust methods for diagnosing where on an ice shelf changes in thickness (here, assumed to occur via increased sub-ice shelf melting) have a significant impact on flux across the grounding line. Our broader goal is to contribute to the understanding of how increased
50 sub-ice shelf melting can be expected to impact the dynamics and stability of real ice sheets.

Below, we first provide a description of the ice sheet model used in our study and the model experiments performed. We then analyze and discuss the experimental results in order to quantify the correlation between easily evaluated, local buttressing metrics and modeled changes in GLF. This leads us to propose and explore an alternative, adjoint-based method for assessing GLF sensitivity to ice shelf thickness perturbations. We conclude with a summary discussion and recommendations.

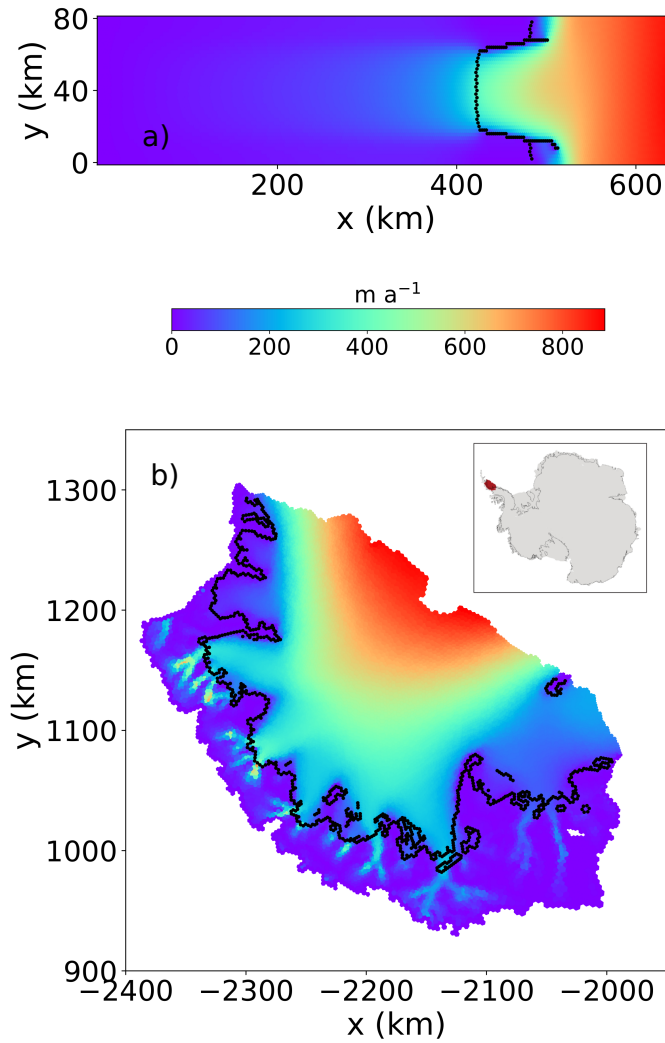


Figure 1. (a) Plan view of surface speed for the MISMP+ and (b) Larsen C Ice Shelf experimental domains. For the Larsen C domain, velocities have been optimized to match observations from Rignot et al. (2011). Black curves indicate the location of the grounding line. The location of Larsen C Ice Shelf is shown as the shaded area in the inset in b). A comparison of modeled and observed ice surface speed is provided in Fig. S1.

2.1 Model description

We use the MPAS-Albany Land Ice model (MALI; Hoffman et al., 2018), which solves the three-dimensional, first-order approximation to the Stokes momentum balance for ice flow. Using the notation of Perego et al. (2012) and Tezaur et al. (2015a), this can be expressed as,

$$\begin{aligned} 60 \quad -\nabla \cdot (2\mu_e \dot{\epsilon}_1) + \rho_i g \frac{\partial s}{\partial x} &= 0, \\ -\nabla \cdot (2\mu_e \dot{\epsilon}_2) + \rho_i g \frac{\partial s}{\partial y} &= 0, \end{aligned} \quad (1)$$

where x and y are the horizontal coordinate vectors in a Cartesian reference frame, $s(x, y)$ is the ice surface elevation, ρ_i represents the ice density, g the acceleration due to gravity, and $\dot{\epsilon}_{1,2}$ are given by

$$\dot{\epsilon}_1 = \begin{pmatrix} 2\dot{\epsilon}_{xx} + \dot{\epsilon}_{yy}, & \dot{\epsilon}_{xy}, & \dot{\epsilon}_{xz} \end{pmatrix}^T, \quad (2)$$

and

$$65 \quad \dot{\epsilon}_2 = \begin{pmatrix} \dot{\epsilon}_{xy}, & \dot{\epsilon}_{xx} + 2\dot{\epsilon}_{yy}, & \dot{\epsilon}_{yz} \end{pmatrix}^T. \quad (3)$$

The “effective” ice viscosity, μ_e in Eq. (1), is given by

$$\mu_e = \gamma A^{-\frac{1}{n}} \dot{\epsilon}_e^{\frac{1-n}{n}}, \quad (4)$$

where γ is an ice stiffness factor, A is a temperature-dependent rate factor, $n = 3$ is the power-law exponent, and the effective strain rate, $\dot{\epsilon}_e$, is defined as

$$70 \quad \dot{\epsilon}_e \equiv \left(\dot{\epsilon}_{xx}^2 + \dot{\epsilon}_{yy}^2 + \dot{\epsilon}_{xx}\dot{\epsilon}_{yy} + \dot{\epsilon}_{xy}^2 + \dot{\epsilon}_{xz}^2 + \dot{\epsilon}_{yz}^2 \right)^{\frac{1}{2}}, \quad (5)$$

where $\dot{\epsilon}_{ij}$ are the corresponding strain-rate components.

Under the first-order approximation to the Stokes equations, a stress free upper surface can be enforced through

$$\dot{\epsilon}_1 \cdot \mathbf{n} = \dot{\epsilon}_2 \cdot \mathbf{n} = 0, \quad (6)$$

where \mathbf{n} is the outward pointing normal vector at the ice sheet upper surface, $z = s(x, y)$. The lower surface is allowed to slide according to the continuity of basal tractions,

$$2\mu_e \dot{\epsilon}_1 \cdot \mathbf{n} + \beta u = 0, \quad 2\mu_e \dot{\epsilon}_2 \cdot \mathbf{n} + \beta v = 0, \quad (7)$$

where β is a spatially variable friction coefficient, $2\mu_e \dot{\epsilon}_{1,2}$ represent the viscous stresses, and \mathbf{u} is the two-dimensional velocity vector (u, v) . The field β is set to zero beneath floating ice and the basal traction is computed with the SEP3 method described in Seroussi et al. (2014). On lateral boundaries in contact with the ocean, the portion of the boundary above sea level is stress free while the portion below sea level feels the ocean hydrostatic pressure according to

$$80 \quad 2\mu_e \dot{\epsilon}_1 \cdot \mathbf{n} = \frac{1}{2} \rho_i g H \left(1 - \frac{\rho_i}{\rho_w} \right) n_1, \quad 2\mu_e \dot{\epsilon}_2 \cdot \mathbf{n} = \frac{1}{2} \rho_i g H \left(1 - \frac{\rho_i}{\rho_w} \right) n_2, \quad (8)$$

where \mathbf{n} is the outward pointing normal vector to the lateral boundary (i.e., parallel to the (x, y) plane), ρ_w is the density of ocean water, and n_1 and n_2 are the x and y component of \mathbf{n} . A more complete description of the MALI model, including the implementations for mass and energy conservation, can be found in Hoffman et al. (2018). Additional details on the momentum
85 balance solver can be found in Tezaur et al. (2015a, b).

2.1.1 GLF computation

The grounding line (GL) is computed as the zero level-set of $\phi(x, y) := \rho_i H(x, y) + \rho_w b(x, y)$, where H and b are the continuous, piece-wise linear finite element fields for the thickness and the bed topography, respectively, defined on a triangulation of the domain at hand. As a consequence, the GL is a piece-wise linear curve, separating grounded ice (where $\phi(x, y) > 0$) from
90 floating ice (where $\phi(x, y) < 0$). The flux F per unit width at a point on the GL is calculated as $F := H\bar{\mathbf{u}} \cdot \mathbf{n}_{GL}$, where $\bar{\mathbf{u}}$ is the vertically averaged velocity, and \mathbf{n}_{GL} is the normal to the GL, pointing towards the floating ice region. The integrated grounding line flux, hereafter GLF, is the line integral of F along the GL and it has units [$\text{m}^3 \text{yr}^{-1}$]. We note that perturbations of the thickness far from the GL affect the GLF only through changes in the velocity field, whereas perturbations of the thickness at triangles intersecting the GL also directly affect ice thickness at the GL and, via the flotation condition, also possibly the
95 position and length of the GL. We further note that ice rises in the model are also surrounded by grounding lines and require no special treatment.

2.2 Model configuration

We apply MALI to experiments on both idealized and realistic marine-ice sheet geometries. For our idealized domain and model state, we start from the equilibrium initial conditions for the MISMIIP+ experiments with a mesh resolution of about
100 2 km, as described in Asay-Davis et al. (2016). For our realistic domain, we use Antarctica’s Larsen C Ice Shelf and its upstream catchment area. For the Larsen C domain, the model state is based on the optimization of the ice stiffness (γ in Eq. (4)) and basal friction (β in Eq. (7)) coefficients in order to provide a best match between modeled and observed present-day velocities (Rignot et al., 2011) using adjoint-based methods discussed in Perego et al. (2014) and Hoffman et al. (2018). The domain geometry is based on Bedmap2 (Fretwell et al., 2013), and ice temperatures, which are used to determine the flow factor and
105 held fixed for this study, are taken from Liefferinge and Pattyn (2013). Mesh resolution is 2 km at the grounding line and coarsens to 4 km near the calving front of the ice shelf and 5 km in the ice sheet interior. Following optimization to present-day velocities, the model is relaxed using a 100-year forward run, providing the initial condition from which the Larsen C experiments are conducted (as discussed below). The domain and initial conditions were extracted from the Antarctica-wide configuration used by MALI for initMIP experiments (Hoffman et al., 2018; Seroussi et al., 2019). Both the MISMIIP+ and
110 Larsen C experiments use 10 vertical layers that are finest near the bed and coarsen towards the surface.

3 Perturbation experiments

To explore the sensitivity of changes in GLF to small, localized changes in ice shelf thickness, we conduct perturbation experiments analogous to those of Reese et al. (2018). Using diagnostic model solutions, we calculate the instantaneous change in GLF for the idealized geometry and initial state provided by the MISMP+ experiment (Asay-Davis et al., 2016). We then
 115 conduct similar experiments for Antarctica’s Larsen C Ice Shelf using a realistic configuration and initial state. The geometries and ice speeds for MISMP+ (steady-state) and Larsen C Ice Shelf (present-day) are shown in Fig. 1.

Our experiments are conducted in a manner similar to those of Reese et al. (2018). We perturb the coupled ice sheet-shelf system by decreasing the ice thickness uniformly by 1 m at ice shelf grid cells (note that we consider the Voronoi grid dual to the Delaunay triangulation used by the finite element solver; every point of the Delaunay triangulation corresponds to a Voronoi
 120 cell), after which we examine the instantaneous impact on kinematics and dynamics (discussed further below). For both the MISMP+ and Larsen C domains, the local ice shelf surface and basal elevations are adjusted following perturbations in order to maintain hydrostatic equilibrium. Lastly, for the MISMP+ 2-km experiments, we note that, in order to save on computing costs, we only perturb the region of the ice shelf for which $x < 530$ km (the area over which the ice shelf is laterally buttressed) and for which $y > 40$ km (due to symmetry about the center line). We do, however, analyze the response to these perturbations
 125 over the entire model domain.

Similar to Reese et al. (2018), we define a GLF response number for our perturbation-based experiments,

$$N_{rp} = \frac{R}{P}, \quad (9)$$

where R is the change in the GLF due to a perturbation in the thickness at a single grid cell (calculated over one year to obtain a dimensionless number), and P is the local volume change associated with the perturbation. The subscript rp denotes the
 130 “response” from “perturbation” experiments. Note that both R and P have units of m^3 so that N_{rp} is dimensionless.

Changes in GLF (quantified by N_{rp}) in response to a local change in ice shelf thickness are expected to occur via changes in ice shelf buttressing, which generally acts to resist the flow of ice across the grounding line. To quantify the local ice shelf buttressing capacity, we calculate a dimensionless buttressing number, N_b , analogous to that from Gudmundsson (2013) and Fürst et al. (2016),

$$135 \quad N_b(\mathbf{n}) = 1 - \frac{T_{nn}}{N_0}, \quad (10)$$

where $T_{nn} := \mathbf{n} \cdot \mathbf{T} \mathbf{n}$ is a scalar measure of the stress normal to the surface defined by \mathbf{n} . The two dimensional stress tensor \mathbf{T} is computed according to the shallow shelf approximation and is defined in Eq. (A6). N_0 is the value of T_{nn} if the ice was removed up to the considered location and replaced with ocean water (or alternatively, the resistance provided by a static, neighboring column of floating ice at hydrostatic equilibrium) defined by

$$140 \quad N_0 := \frac{1}{2} \rho_i g \left(1 - \frac{\rho_i}{\rho_w} \right) H, \quad (11)$$

with ρ_i and ρ_w being the densities of ice and ocean water, respectively. For the MISMP+ experiment, $\rho_i=918 \text{ kg m}^{-3}$ and for the Larsen C experiment, $\rho_i=910 \text{ kg m}^{-3}$. For both experiments, $\rho_w=1028 \text{ kg m}^{-3}$. We elaborate further on the calculation of

the buttressing number in Appendix A. While Gudmundsson (2013) chose the unit vector \mathbf{n} to be normal to the grounding line to define the “normal” buttressing number, Fürst et al. (2016) extended his definition to the ice shelf by examining $N_b(\mathbf{n})$ for \mathbf{n} along the ice flow direction and along the direction of the second principal stress. Here, we explore the connection between changes in grounding line flux (quantified by N_{rp}), sub-shelf melting, and local buttressing on the ice shelf (quantified by N_b) corresponding to arbitrary \mathbf{n} (in order to consider all possible relationships on the ice shelf). Note that we do not discuss the tangential buttressing number defined by Gudmundsson (2013); hereafter, we use “buttressing number” to refer exclusively to the “normal buttressing number”, as defined above.

150 4 Results

4.1 Correlation between buttressing and changes in GLF

A decrease in ice shelf buttressing tends to lead to an increase in GLF (e.g., Gagliardini et al., 2010, also see Fig. 2a) and intuitively we expect that the GLF should be relatively more sensitive to ice shelf thinning in regions of relatively larger buttressing. We aim to better understand and quantify the relationship between the local ice shelf buttressing “strength” in a given direction (characterized by N_b) and changes in GLF (characterized by N_{rp}). A reasonable hypothesis is that, for a given ice thickness perturbation, the resulting change in the GLF is proportional to the buttressing number at the perturbation location. In Fig. 2, we show the results from all (730) perturbation experiments for MISMIP+, and the corresponding N_{rp} and N_b values. We show values of N_b for three different directions, corresponding to the choice of \mathbf{n} in Eq. (10): the first principal stress direction (\mathbf{n}_{p1}), the second principal stress direction (\mathbf{n}_{p2}), and the ice flow direction (\mathbf{n}_f). In the discussion below, we frequently refer to these three directions when discussing the buttressing number. In agreement with the findings of Fürst et al. (2016), the largest values for N_b occur when it is calculated in the \mathbf{n}_{p2} direction. While there appears to be a qualitatively reasonable spatial correlation between the magnitude of N_{rp} and N_b when the latter is calculated in the \mathbf{n}_{p2} and \mathbf{n}_f directions (and less so when calculated in the \mathbf{n}_{p1} direction), in Fig. 3 we show that there is no clear relationship between the response number N_{rp} and the buttressing number N_b calculated along any of these directions, at least for the case where we consider all points on the ice shelf.

In Fig. 4, we show correlations between the modeled value of N_{rp} and N_b where we ignore points meeting the following criteria: (i) points where the ice shelf becomes unconfined ($x > 480$ km); (ii) points within 2 cells from the GL; (iii) points where shear stresses are large according to the metric,

$$m_s = \frac{|\sigma_{p1} - \sigma_{p2}|}{|\sigma_{p1} + \sigma_{p2}|}, \quad (12)$$

where σ_{p1} and σ_{p2} are the first and second principal normal stresses, respectively, and m_s is the ratio of the maximum shear stress to the mean normal stress. For the case of (i), a good correlation between N_b and N_{rp} is not expected for unconfined flow where buttressing is insignificant (Van Der Veen, 2013). For the case of (ii), complications near the grounding line (e.g., grounding line movement and geometry change associated with thickness perturbations, as noted in 2.1.1) may give incorrect GLF response numbers. For the case of (iii), we expect a relatively poor correlation between N_b and N_{rp} for locations

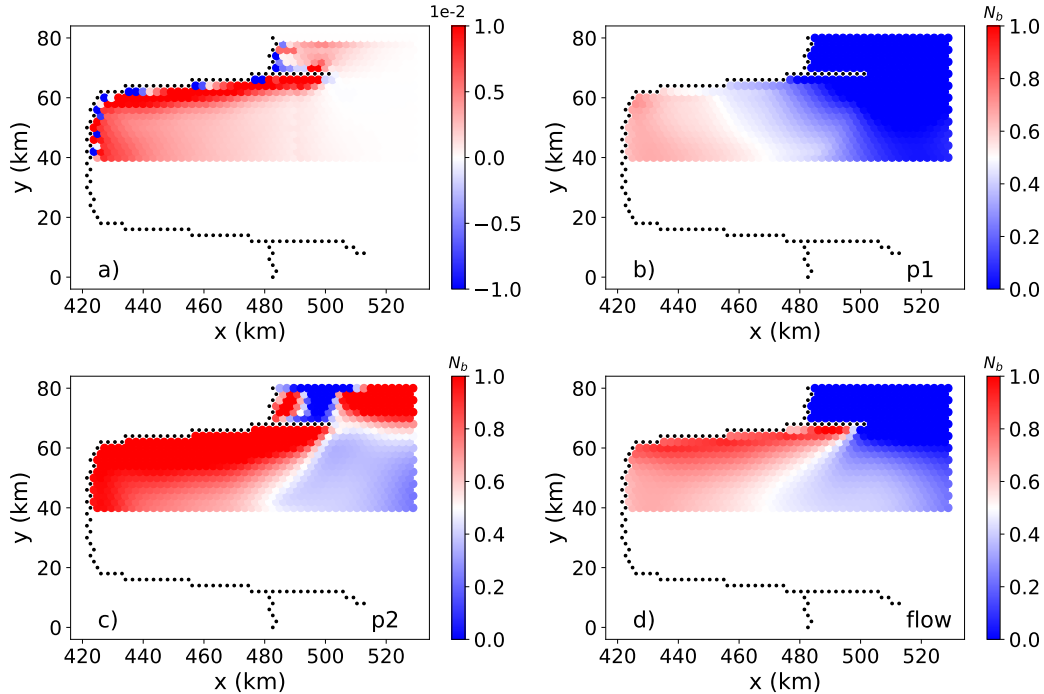


Figure 2. GLF number and buttressing number for each of the 730 perturbed grid cells in the MISIMIP+ experiments. (a) The spatial distribution of the GLF response number, N_{rp} . (b-d) The spatial distribution of the buttressing number, N_b , corresponding to directions (b) \mathbf{n}_{p1} , (c) \mathbf{n}_{p2} , and (d) \mathbf{n}_f . Black dots indicate grid cells located along the grounding line. The negative N_{rp} values in (a) correspond to a few partially-grounded cells in the vicinity of the GL, where the GLF can be reduced by ice shelf thinning. Here the colorbars for (a)–(d) do not show the full data range. Note that the negative GLF numbers in panel (a) are due to the nonlinear impacts of changes in both ice thickness and velocity at the GL.

175 where buttressing occurs primarily via lateral drag, which will be poorly captured by a stress metric (i.e., buttressing number) associated with a single direction. In a principal stress framework, shear stress is described by perpendicular normal stresses of opposite sign. Applying this metric means that we only evaluate correlations between N_b and N_{rp} for points where m_s from Eq. (12) is < 1 (i.e., where normal stress is dominant over shear stress; see also Fig. S2). When applying criteria (i)–(iii) above as a spatial filter, the number of points considered is reduced (Fig. 4a) and stronger correlations between N_{rp} and N_b emerge.

180 In particular, a stronger correlation between N_{rp} and N_b occurs when N_b is calculated using \mathbf{n}_{p1} (Fig. 4b) or \mathbf{n}_f (Fig. 4d), relative to when using \mathbf{n}_{p2} (Fig. 4c).

4.2 Directional dependence of buttressing

The buttressing number at any perturbation point depends on T_{nn} , which in turn depends on the chosen direction of the normal vector, \mathbf{n} (Eq. (10)). Fürst et al. (2016) calculated N_b using \mathbf{n}_f and \mathbf{n}_{p2} and chose the latter – the direction corresponding to

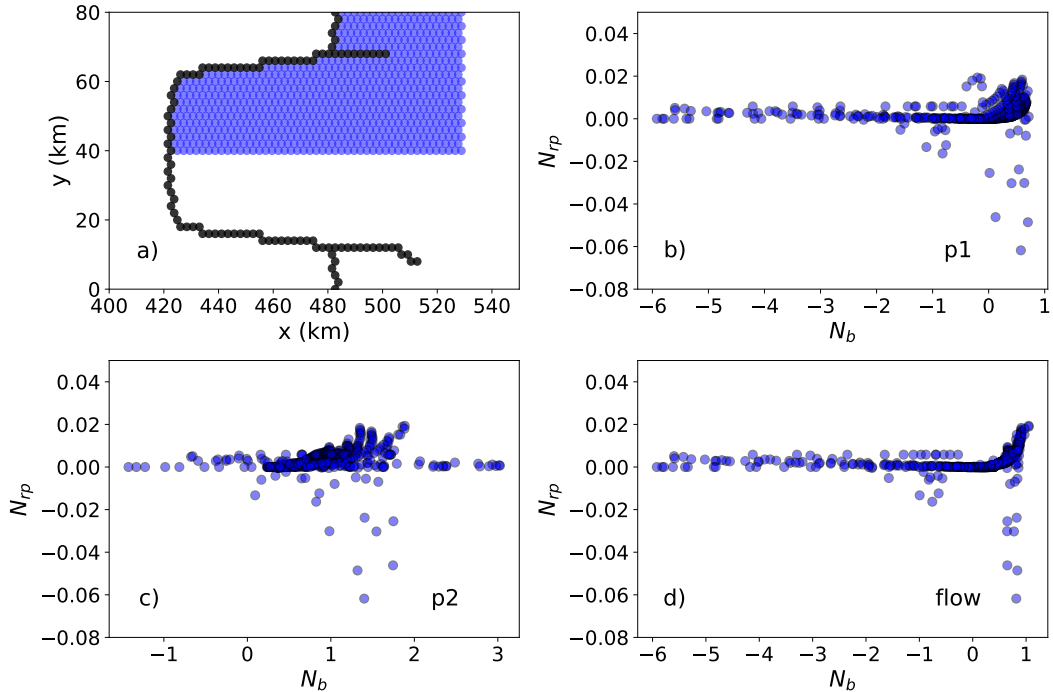


Figure 3. (a) Blue dots represent the locations of all perturbation points analyzed (730) for the $N_{rp} : N_b$ relation analysis. Black dots indicate grid cells located along the grounding line. (b-d) Modeled N_{rp} versus buttressing number N_b calculated along (b) \mathbf{n}_{p1} , (c) \mathbf{n}_{p2} , and (d) \mathbf{n}_f .

185 the second principal stress (the maximum compressive stress or the least extensional stress) – to quantify the local value of “maximum buttressing” on an ice shelf. In Fig. 5a, we plot the linear-regression correlation coefficients (r) for the $N_{rp} : N_b$ relationship where the direction of \mathbf{n} used in the calculation of T_{nn} varies continuously from $\Delta\phi = 0^\circ$ – 180° relative to \mathbf{n}_{p1} (we also show how the buttressing number N_b varies as a function of direction in Fig. S3). We find large correlation coefficients ($r > 0.9$) when N_b is aligned closely with \mathbf{n}_{p1} ($\Delta\phi = 0^\circ$ or 180°) and the smallest correlation coefficient ($r < 0.5$) when N_b is aligned with \mathbf{n}_{p2} ($\Delta\phi = 90^\circ$). Similar conclusions can be reached when examining the variation of r with respect to the ice flow direction (Fig. 5b), where correlations are phase shifted by approximately 50° counter-clockwise relative to Fig. 5a. Clearly, the best correlation occurs along a direction somewhere between \mathbf{n}_{p1} and \mathbf{n}_f . Note that we do not see an exact match between Fig. 5a and Fig. 5b if we shift the angle by 50° because the angular difference between \mathbf{n}_{p1} and \mathbf{n}_f varies for the perturbation locations analyzed.

195 Fürst et al. (2016) posit that $N_b(\mathbf{n}_{p2})$ provides a good local buttressing metric and chose it for identifying regions of maximum buttressing on an ice shelf with the goal of identifying “passive” ice that can be removed without tangibly affecting the remaining ice. While our results also show that buttressing is greatest in the direction of the second principal stress (which follows from the definitions of the second principal stress and the buttressing number, see also Fig. S3), we find that buttressing

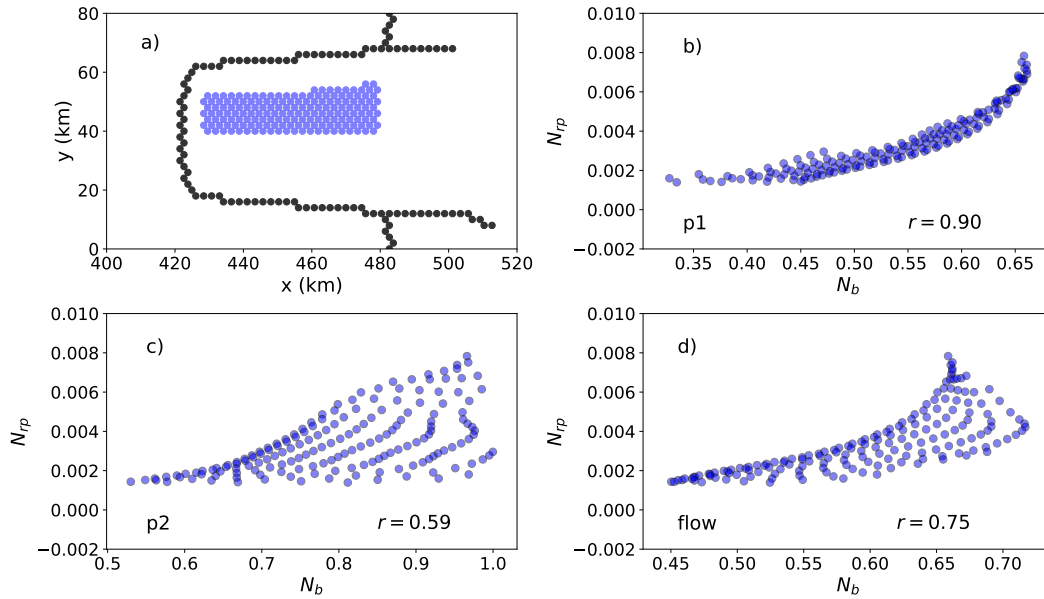


Figure 4. (a) Blue dots represent the locations of all perturbation points analyzed (168) for the $N_{rp} : N_b$ linear regression analysis, based on the filtering criteria discussed in Section 4.1. Black dots indicate grid cells located along the grounding line. (b-d) Modeled N_{rp} versus buttressing number N_b calculated along (b) \mathbf{n}_{p1} , (c) \mathbf{n}_{p2} , and (d) \mathbf{n}_f . The correlation coefficient for each modeled N_{rp} versus N_b is given by r .

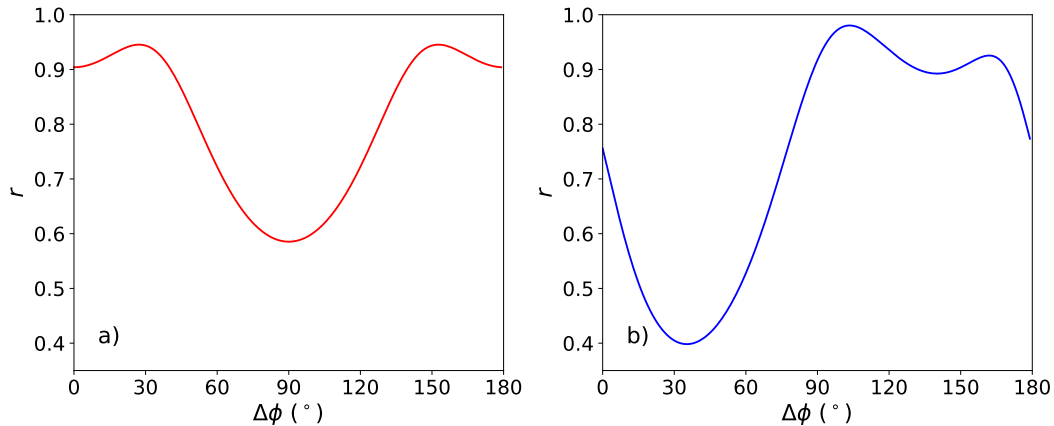


Figure 5. Correlation coefficients for the linear regression relationship of $N_{rp} : N_b$ where \mathbf{n} is rotated counterclockwise by $\Delta\phi$ degrees relative to (a) \mathbf{n}_{p1} and (b) \mathbf{n}_f . The perturbation points analyzed here are the same as in Fig. 4a.

in this direction is not useful for predicting changes in GLF; compared to $N_b(\mathbf{n}_{p2})$, $N_b(\mathbf{n}_{p1})$ and $N_b(\mathbf{n}_f)$ both show a better correlation with changes in GLF via local, sub-ice shelf melt perturbations. We discuss these differences further in Section 5.

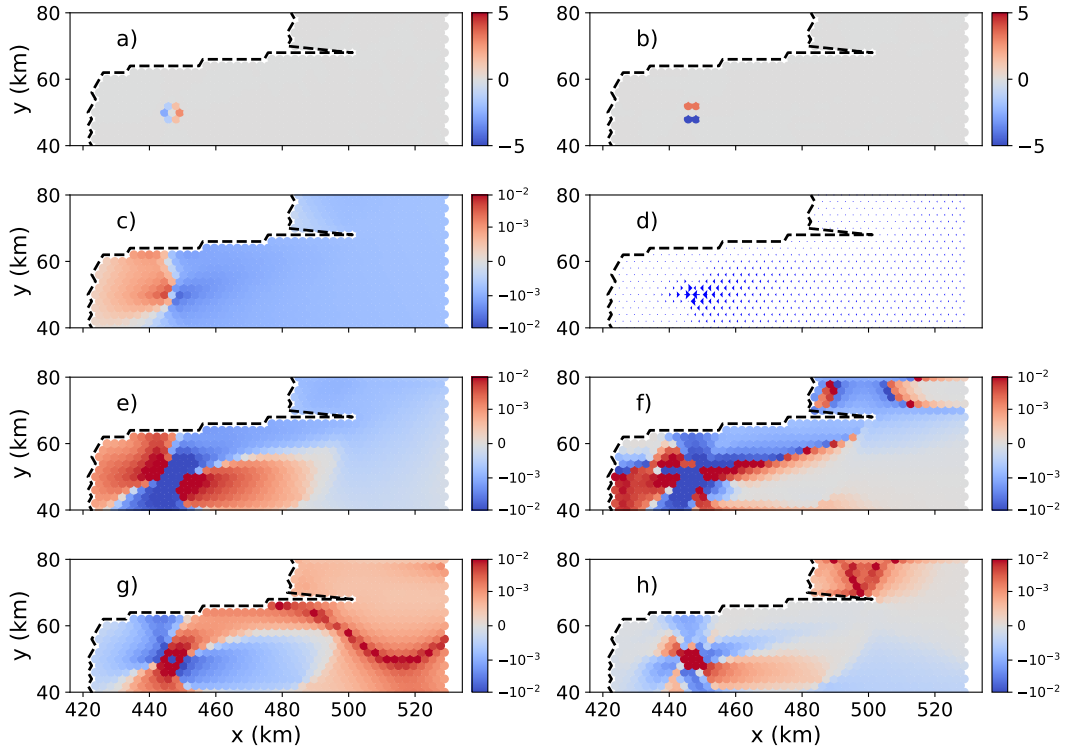


Figure 6. An example of the local change (ratio, in %) in (a) the ice thickness gradient in x , (b) ice thickness gradient in y , (c) ice speed, (d) ice velocity (relative), (e, f) principal strain rates, and (g, h) buttressing number following a local perturbation to the ice shelf thickness. In (e) and (g), changes (colors) are associated with the \mathbf{n}_{p1} direction and for (f) and (h) changes are associated with the \mathbf{n}_{p2} direction.

4.3 Perturbation impacts: local, far-field, and integrated changes

We now look more carefully at thickness perturbations on the ice shelf in terms of their local, far-field, and integrated impacts on changes in geometry, velocity, stress, buttressing, and GLF.

4.3.1 Local perturbation impacts

205 Local thickness perturbations on the ice shelf alter the local ice thickness gradient; on the upstream side of the perturbation, it becomes more negative while on the downstream side it becomes less negative (Fig. 6a, b). These thickness gradient changes increase the ice speed immediately upstream from the perturbation and decrease it immediately downstream of the perturbation (Fig. 6c), resulting in anomalous flow convergence towards the perturbation location (Fig. 6d). The resulting impacts on the principal strain rates (and thus the principal stresses) are increased compression (or decreased extension) along both principal
 210 directions (Fig. 6e, f) and, via Eq. (10), a corresponding increase in the local value of N_b along both principal stress directions

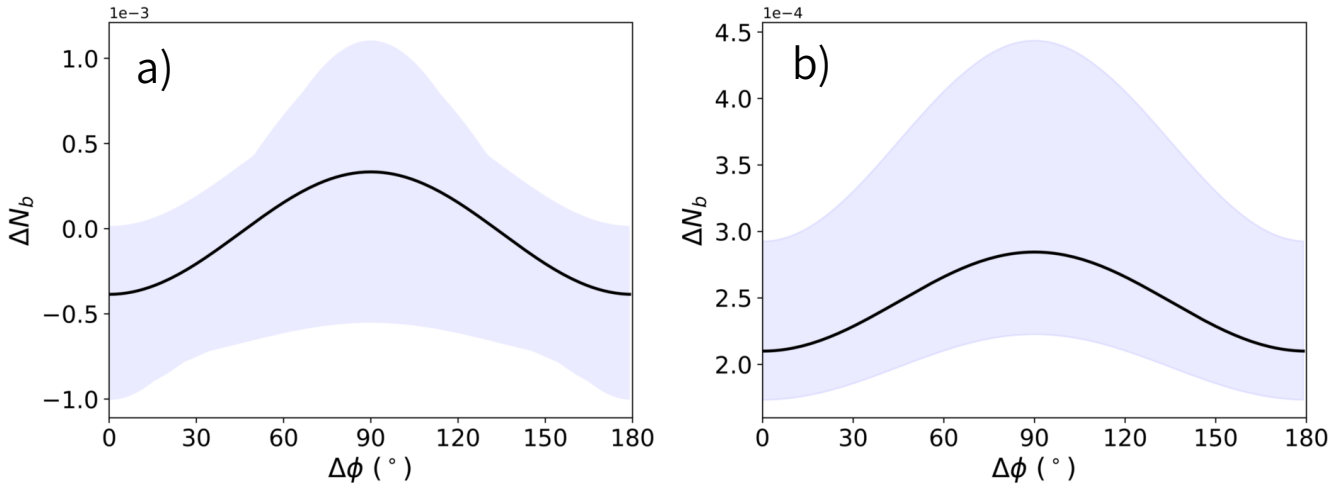


Figure 7. The change in buttressing number, ΔN_b , at and near to ice shelf thickness perturbations. In (a), the change at the perturbation location is shown and in (b) the mean change in all immediately neighboring cells is shown. Changes in buttressing are calculated along the direction $\Delta\phi$, rotated counterclockwise relative to the \mathbf{n}_{p1} direction. The points analyzed include those in Fig. 4a, which are shown as the shaded area, with the solid curve representing their mean value.

(Fig. 6g, h). These spatial patterns of change are robust for a number of different perturbation points on the ice shelf (see Figs. S4 and S5 in the Supplementary Material).

An important caveat applies to the grid cell associated with the location of the perturbation itself, where a decrease in N_b is seen, sometimes for only the \mathbf{n}_{p1} direction but other times for both principal directions (Fig. S5). In Fig. 7, we quantify the local (at the perturbation location; Fig. 7a) and neighboring (immediately surrounding the perturbation location; Fig. 7b) changes in N_b for all of the points analyzed in Fig. 4 and for all possible directions. From Fig. 7, we make two conclusions: 1) the local change in N_b is generally more positive along the \mathbf{n}_{p2} direction (indicating a local *increase* in buttressing accompanying a thickness perturbation) and 2) the local and neighboring changes in buttressing are often inconsistent (i.e., a *decrease* in N_b at a particular grid cell coincides with an *increase* in N_b in the neighboring cells). The first conclusion would seem to argue against using $N_b(\mathbf{n}_{p2})$ for quantifying local changes in buttressing in terms of their broader impacts on GLF (because, surprisingly, local thinning perturbations are more likely to indicate a local *increase* in buttressing along the \mathbf{n}_{p2} direction). The second conclusion suggests that analysis over wider spatial scales may be necessary for a consistent understanding of how local ice shelf perturbations impact GLF.

4.3.2 Far-field perturbation impacts

Away from the immediate vicinity of ice shelf thickness perturbations (i.e., beyond the grid cell where perturbations are applied and its immediate neighbors), the resulting changes are more uniform and easier to interpret. The broader pattern of increased ice speed upstream from a perturbation location can be seen to extend spatially and diffuse with increased distance

(Fig. 6c). Similar can be observed with respect to changes in principal strain rates and buttressing, at least for the \mathbf{n}_{p1} direction (Figs. 6e and g), where a wide swath of increased extension and decreased local buttressing (as quantified by reductions in $N_b(\mathbf{n}_{p1})$) coincides with the region of increased ice speed extending upstream to the grounding line. This implied causality – a reduction in buttressing on the shelf leads to an increase in GLF upstream – is consistent with our understanding of ice shelf buttressing. Importantly, we note that a similar understanding based on changes in the \mathbf{n}_{p2} direction (Figs. 6f and h) is much less straightforward due to more complicated spatial patterns and no obvious consistency between reductions in $N_b(\mathbf{n}_{p2})$ and the increases in ice speed that would lead to a corresponding increase in GLF. This interpretation of the far-field effects of local ice shelf perturbations is consistent when perturbations are applied at a number of different locations on the ice shelf (see Figs. S4 and S5 in the Supplementary Material).

A reasonable hypothesis is that the apparent correlation between $N_b(\mathbf{n}_{p1})$ and N_{rp} in Fig. 4b arises because of the connection, discussed above, between local thickness perturbations, far-field changes in principal stresses and buttressing along the \mathbf{n}_{p1} direction, and increases in ice speed upstream of the perturbation. Similarly, the lack of such a clear connection for local perturbations and principal stresses and buttressing along the \mathbf{n}_{p2} direction may account for the relatively poorer correlation between $N_b(\mathbf{n}_{p2})$ and N_{rp} shown in Fig. 4c. Next, we explore how these far-field changes are expressed at the grounding line.

4.3.3 Perturbation impacts on buttressing and ice flux at the grounding line

To understand how local perturbations in ice shelf thickness impact GLF, we now examine changes in the buttressing number and ice speed at and normal to the grounding line. To quantify this relationship, we define Υ_{gl} ,

$$\Upsilon_{gl} = \text{Corr}(\Delta\mathbf{N}_b, \Delta\mathbf{u}) = \frac{\text{cov}(\Delta\mathbf{N}_b, \Delta\mathbf{u})}{s(\Delta\mathbf{N}_b)s(\Delta\mathbf{u})}, \quad (13)$$

where $\Delta\mathbf{N}_b = \mathbf{N}_{bp} - \mathbf{N}_{bc}$ and $\Delta\mathbf{u} = \mathbf{u}_p - \mathbf{u}_c$ and with the subscripts p and c denoting the “perturbed” and “control” (i.e., initial) model states, respectively. $\Delta\mathbf{N}_b$ and $\Delta\mathbf{u}$ denote vectors of the *changes* in the buttressing number and ice speed normal to the GL, respectively, for all GL cells along the main trunk of the ice stream (red points in Fig. 8). Υ_{gl} , a correlation coefficient, is an integrated measure of the consistency between the magnitude and the sign of the change in buttressing number and ice speed between the control and perturbation experiments, with cov and s representing the covariance and the standard deviation, respectively.

By plotting values of Υ_{gl} mapped to their respective perturbation locations on the ice shelf (Fig. 8), we show there is generally a *negative* correlation between speed and buttressing at the GL: in response to a thickness perturbation on the ice shelf, buttressing *decreases* and speed (and hence flux) across the GL *increases*, in line with our general understanding of buttressing. In Fig. 8a, we show a reference case for which T_{nn} in Eq. (10) (and hence in Eq. (13)) is calculated normal to the grounding line. In this case, the N_b values in Eq. (13) are calculated along the GL as defined by Gudmundsson (2013) ($\Upsilon_{gl} = \Upsilon_{gl}(\mathbf{n}_{gl})$), where \mathbf{n}_{gl} is the direction normal to the grounding line). In Fig. 8b and c, we show $\Upsilon_{gl}(\mathbf{n}_{p1})$ and $\Upsilon_{gl}(\mathbf{n}_{p2})$, respectively. As expected, the correlation is strongly negative for $\Upsilon_{gl}(\mathbf{n}_{gl})$ (Fig. 8a) and we find that $\Upsilon_{gl}(\mathbf{n}_{p1})$ is a close match (Fig. 8b). While much of the shelf under consideration also shows a negative correlation for $\Upsilon_{gl}(\mathbf{n}_{p2})$, the correlations are

260 generally weaker and there are regions near the center of the shelf, and closer to the grounding line where the correlation switches sign, implying an increase in buttressing (as calculated in that direction) accompanying an increase in GLF (Fig. 8c).

In addition to the results for the three discrete normal directions discussed above, a continuous analysis of Υ_{gl} as a function of the normal stress direction is shown in Fig. 9 where we plot Υ_{gl} at each perturbation point and for *all* directions in the range of $\Delta\phi = 0-180^\circ$ relative to \mathbf{n}_{p1} . This correlation is generally negative and stronger for buttressing numbers calculated
265 near the \mathbf{n}_{p1} direction ($\Delta\phi$ closer to 0° or 180°) and weaker (or even strongly positive) approaching the \mathbf{n}_{p2} direction. This analysis connects the local perturbations and far-field impacts described above with changes in integrated GLF, providing a further means for understanding the correlation between $N_b(\mathbf{n}_{p1})$ and N_{rp} in Fig. 4b.

4.3.4 Summary of local versus integrated impacts of ice shelf perturbations

The changes in ice speed and buttressing at the grounding line quantified by Figs. 8 and 9 must be the result of perturbations
270 initiated on the ice shelf that have propagated (here, instantaneously) to the grounding line, where increases in speed are associated with increased extension along \mathbf{n}_{p1} and, according to Eq. (10), decreased buttressing associated with the \mathbf{n}_{p1} direction. Intuitively, these increases in ice speed at the grounding line must be triggered by the loss of buttressing on the shelf, initiated here via small and highly localized ice thickness (thinning) perturbations. As shown and argued above, however, it is difficult to understand the integrated impacts of these perturbations on GLF based on changes in locally derived quantities alone, in particular, the locally derived buttressing number, N_b . One would come to very different conclusions regarding how a perturbation
275 impacts local buttressing depending on both the spatial scale of the area around a perturbation being examined and the principal direction used for calculating N_b (e.g., Figs. 7a and b). Over wider spatial scales, however, we do find consistency between the impacts of local perturbations on geometry, stresses, local buttressing, ice speed, and changes in GLF (Figs. 6, 8, 9). While we hypothesize that it is this consistency that lies behind the apparent correlation between N_b and N_{rp} in Fig. 4b, we still lack the
280 detailed physical understanding behind that correlation that would be required for us to apply it with confidence.

Further, we show in the Supplementary Material and Table S01 that the correlation between N_b and N_{rp} may be spurious, perhaps due to correlations with some other common variable. Finally, in the next section we show that this tenuous correlation between N_b and N_{rp} breaks down almost entirely when applied to a realistic ice shelf.

4.4 Application to Larsen C Ice Shelf

285 We apply a similar set of analyses, as discussed above for the MISMIIP+ domain, to a realistic, Larsen C ice shelf domain. For this domain, with complex geometry and spatially variable ice temperature (and associated ice rigidity), the relationship between $N_b(\mathbf{n}_{p1})$ and N_{rp} becomes much weaker relative to that for the MISMIIP+ domain. Fig. 10 shows that using the shear metric m_s (Eq. (12)) to filter locations reduces the scatter between $N_b(\mathbf{n}_{p1})$ and N_{rp} . However, even when retaining only points with low shear contributions, the relationship is nonlinear without a clear functional form. Furthermore, restricting analysis to
290 the low shear regions where the relationship is stronger excludes the majority of the ice shelf, including most of the regions of where the GLF response number is large (see also Fig. 13a below). We find a similar result when coarsening the analysis to use 20×20 km boxes for the analysis, as was done for the N_{rp} calculations performed by Reese et al. (2018); a strong correlation

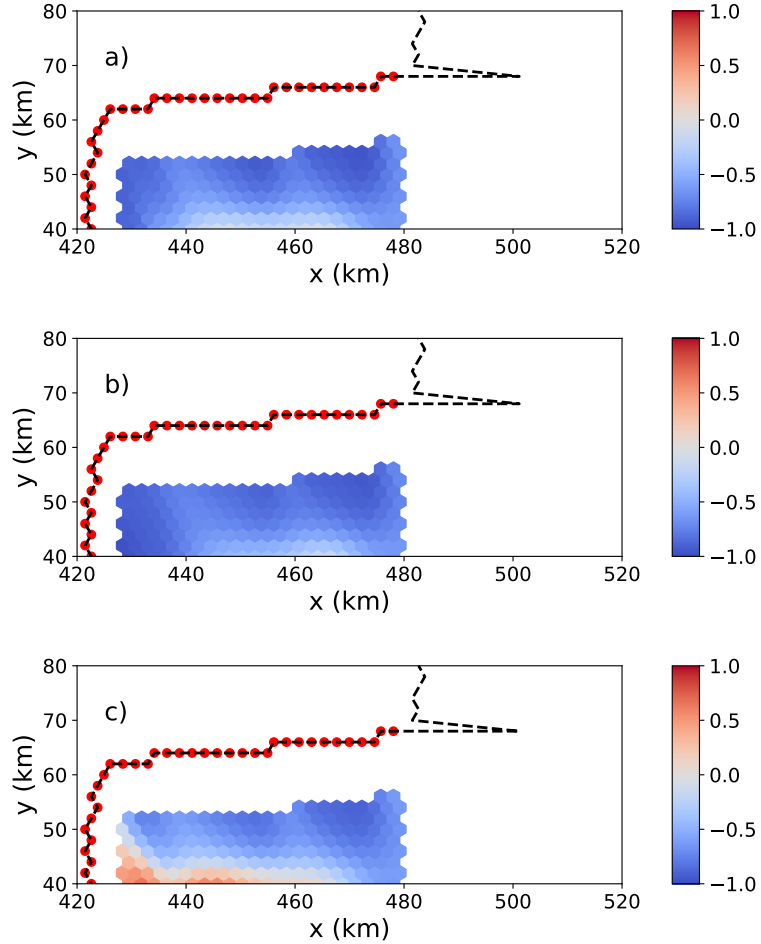


Figure 8. Spatial distribution of the correlation coefficient Υ_{g1} from Eq. (13) over the MISMP+ domain for buttressing number changes calculated parallel to (a) \mathbf{n}_{gl} , (b) \mathbf{n}_{p1} and (c) \mathbf{n}_{p2} (colors). Υ_{g1} is a measure of the correlation between changes in buttressing number and ice speed along the grounding line. The black-dashed line represents the grounding line and the red dots indicate the area of the grounding line for which values of Υ_{g1} are calculated for each perturbation on the ice shelf, as shown in Fig. 4a.

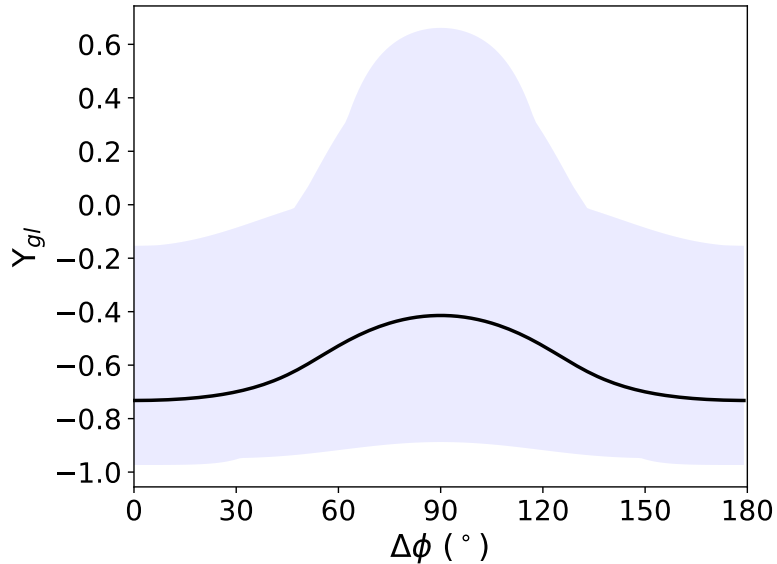


Figure 9. Correlation between the change in buttressing number and the change in ice speed across the grounding line (i.e., Υ_{gl} from Eq. (13)) for the entire MISMIP+ grounding line. The horizontal axis shows how Υ_{gl} varies as a function of the direction \mathbf{n} used to define the normal stress, rotated counterclockwise from \mathbf{n}_{p1} by $\Delta\phi$. Values from the maps in Figs. 8a and b plot at $\Delta\phi$ values of 0 and 90 degrees, respectively. Thus, the blue shaded region represents all possible maps for all possible values of buttressing direction. The thick black curve represents the mean value of Υ_{gl} for any given map.

exists for only a small area near the center of the ice shelf (Fig. S6). Even weaker relationships are found for the \mathbf{n}_{p2} and \mathbf{n}_f directions. Thus, while there clearly is some link between $N_b(\mathbf{n}_{p1})$ and N_{rp} for a realistic ice shelf, it is far too tenuous to be
 295 used in a predictive way and likely differs across and between ice shelves.

Overall, for a realistic ice shelf like Larsen C with a complex geometry and flow field, we find it even more difficult to demonstrate robust relationships between the local ice shelf buttressing number and changes in GLF. This is, at least in part, likely due to the fact that, for more complex and realistic domains, there is no dominant direction of buttressing controlling ice flux across the grounding line. These findings further diminish our confidence in using locally derived buttressing numbers for
 300 assessing the sensitivity of GLF to changes on the ice shelf. For this reason, we explore an alternative and more robust method for quantifying how ice shelf thickness perturbations affect flux at the grounding line.

4.5 Adjoint sensitivity

While our goal throughout this study has been to find a simple and robust metric for diagnosing GLF sensitivity to ice shelf thickness perturbations, the challenges and complications discussed above suggest that this may not be possible. This motivates
 305 our investigation of a wholly different approach, which provides a GLF sensitivity map analogous to that from Reese et al. (2018), instead of seeking for a simple buttressing number indicator to predict the GLF sensitivity. But rather than computing

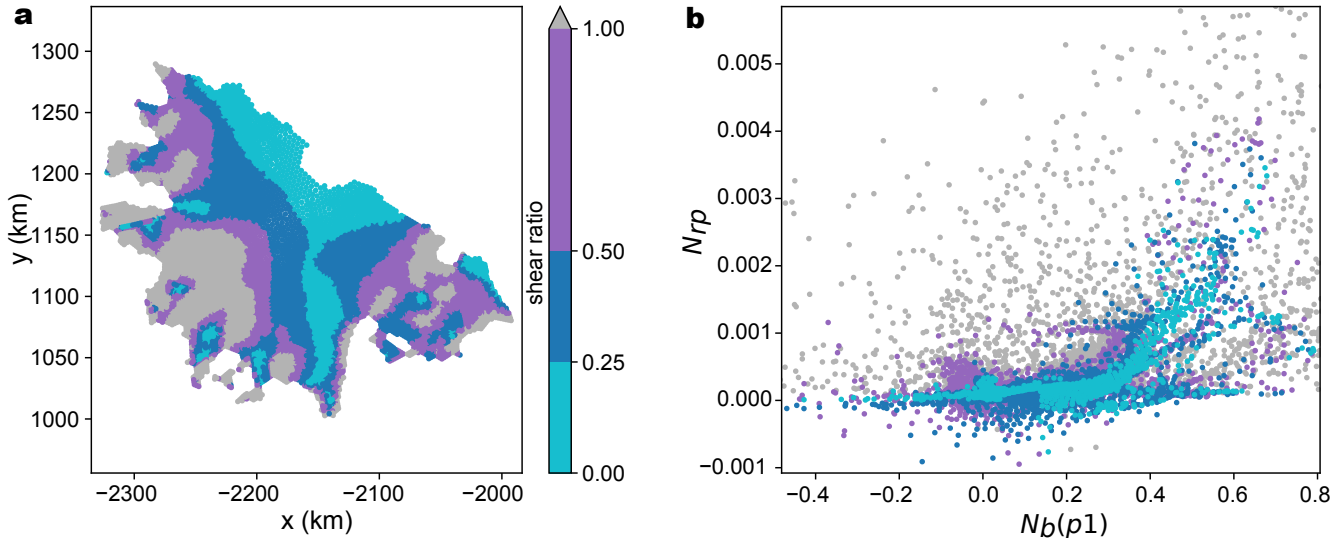


Figure 10. a) Larsen C model domain colored by the shear metric, m_s (Eq. (12)). b) Scatter plot of $N_b(p1)$ and N_{rp} colored by different values of m_s .

the GLF change due to a perturbation applied individually at each of n model grid cells (thus requiring n diagnostic solves), we use an adjoint-based method that allows for the computation of the sensitivity at all n grid cells simultaneously at the cost of a single adjoint-model solution. Briefly, this method involves the solution of an auxiliary linear system (the adjoint system) to compute the so-called Lagrange multiplier, a variable with the same dimensions as the forward-model solution for the ice velocity. Here, the matrix associated with the system is the transpose of the Jacobian of the first-order approximation to the Stokes flow model (Perego et al., 2012). In addition, the adjoint method requires computation of the partial derivatives of the first-order model residual and the GLF with respect to the velocity solution and the ice thickness. Here, we compute the Jacobian and all the necessary derivatives using automatic differentiation (Tezaur et al., 2015a). Additional details of the adjoint-based method and calculations are given in Appendix C.

A similar approach has been proposed by Goldberg et al. (2019). That work primarily assessed the adjoint sensitivity of the volume above floatation with respect to sub-ice shelf melting of Dotson and Crosson ice shelves in West Antarctica. In contrast to our approach, Goldberg et al. (2019) compute *transient* sensitivities because their quantity of interest (volume above floatation) is time dependent.

The adjoint-based sensitivity has units of volume flux per year per meter of ice thickness perturbation ($\text{m}^2 \text{yr}^{-1}$). We nondimensionalize this value, dividing it by the area of the perturbed cell and multiplying it by the one year period over which we consider the perturbation, so that it is dimensionless and comparable to N_{rp} , and refer to it as N_{ra} (where the subscript a is for “adjoint”). In Figs. 11 and 12, we demonstrate the application of this method to the MISMIP+ and Larsen C domains by comparing GLF sensitivities deduced from 730 and 1000 points (i.e., from the respective perturbation experiments discussed

325 above for the MISMIP+ and Larsen C domains, respectively) with those deduced from a single adjoint-based solution. The comparison demonstrates that the two approaches provide a near exact match.

As might be expected based on the discussion above, the two methods disagree in regions very near to the grounding line (see Fig. 13c). This discrepancy is likely a consequence of large non-linearities near the grounding line, as suggested by the fact that the agreement between the two methods improves as the size of the perturbation decreases (from 10 m to 0.001 m; see Fig. 13), the only change being the magnitude of the applied perturbation). This might be exacerbated by the sliding law adopted in this work, which results in abrupt changes in the basal traction across the grounding line. Other sliding laws, e.g. Brondex et al. (2017), allow for a smoother transition at the grounding line and might mitigate this problem. We also note that some isolated cells adjacent to the grounding line exhibit negative sensitivities (a *decrease* in ice flux following a *decrease* in ice thickness), opposite those exhibited by the rest of the ice shelf. We attribute these to partially grounded cells, for which the sensitivity may be more akin to that expected for grounded ice (i.e., a direct relationship between ice thickness and ice flux).

The adjoint sensitivity map represents a linearization of the GLF response to thickness perturbations. As long as the perturbations are small enough, one can approximate the GLF response by multiplying the sensitivity map by the thickness perturbation. Comparison of N_{ra} and N_{rp} for different perturbation sizes (Fig. 13) suggests that this is reasonable for perturbations on the order of <10 m for points on the ice shelf that are not too close to the GL. At the same time care should be taken when interpreting the sensitivities – based on either the perturbation- or adjoint-based methods – in the vicinity of grounding lines. This is especially important when considering that the near-grounding-line region is also that with the largest sensitivities (Figs. 11a and 12a). Because these sensitivities may be inaccurate, they provide an argument for applying high spatial resolution near the grounding line; coarse resolution near the grounding line will extend the region over which inaccurate sensitivities may be assessed. More accurately assessing the sensitivities near the grounding line may require the application of perturbations with both magnitudes and spatial scales that are more realistic than the infinitesimal, highly localized perturbations explored here.

The adjoint method provides sensitivity maps over the entire ice shelf, including around islands, promontories, and along the grounding line itself, which is generally the part of the ice shelf where the GLF is the most sensitive to thickness perturbations (e.g., see Figs. 11a and 12a and Fig. 1 in Reese et al. 2018). Thus, despite the added complexity in its computation, the adjoint-based method provides significant advantages over the simpler perturbation-based analysis methods discussed above.

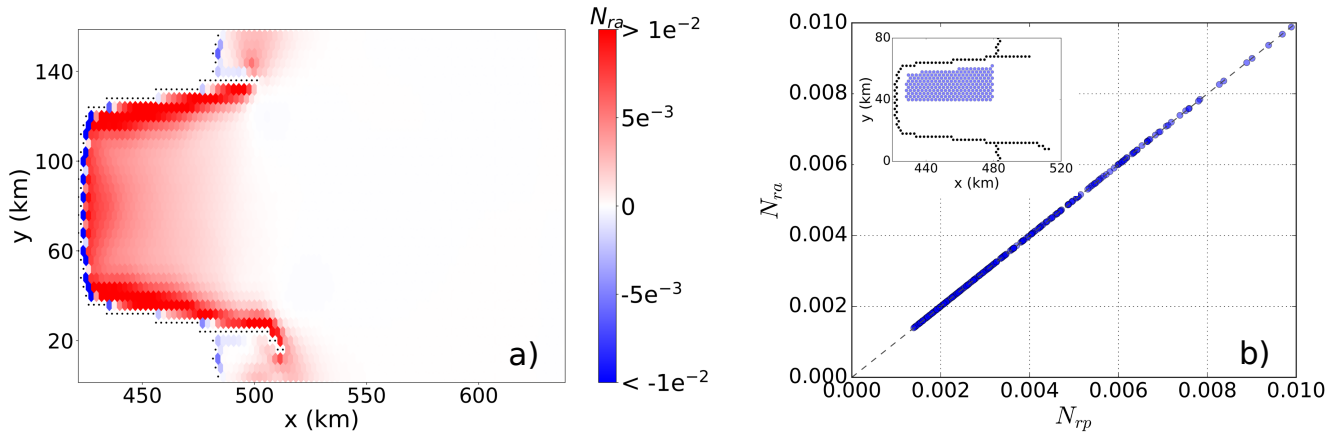


Figure 11. (a) Grounding line flux sensitivity for the MISIP+ domain derived from the adjoint model approach. (b) Perturbation- (N_{rp} ; x -axis) versus adjoint-based (N_{ra} ; y -axis) sensitivities plotted against one another (perturbation locations are shown by circles in the inset, where the grounding line grid cells are shown by the black dots.)

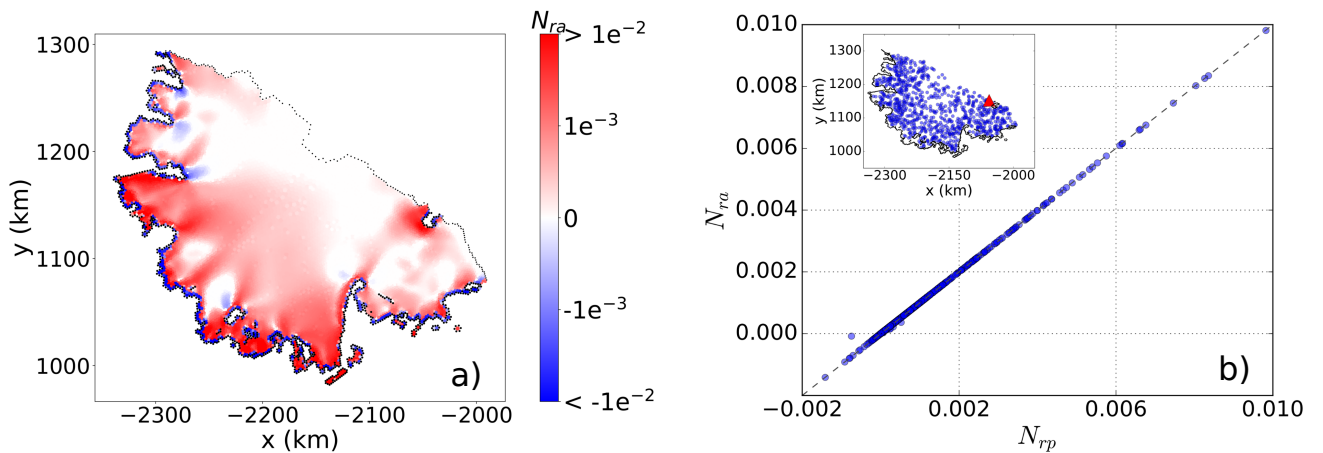


Figure 12. (a) Grounding line flux sensitivity for the Larsen C domain derived from the adjoint model approach. (b) Perturbation- (N_{rp} ; x -axis) versus adjoint-based (N_{ra} ; y -axis) sensitivities plotted against one another (perturbation locations are shown by circles in the inset, where the one outlier in b) is at the calving front (red triangle), and the grounding line in is shown by the black curve.)

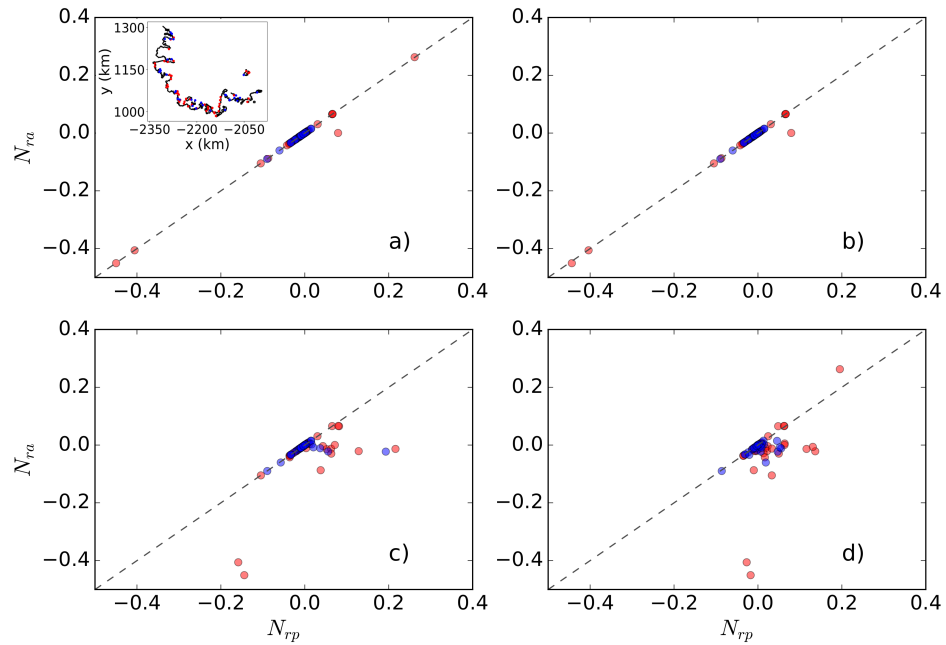


Figure 13. Comparisons between perturbation- and adjoint-based sensitivities (N_{rp} and N_{ra} , respectively) for ice thickness perturbation of (a) 0.001 m, (b) 0.01 m, (c) 1 m and (d) 10 m for perturbation points near the grounding line (<3 km) indicated by the dots on the inset map in (a). Red dots represent grid cells next to the grounding line and blue dots represent grid cells on the ice shelf proper.

The current interest in better understanding the controls on the MISI is due to the potential for future (and possibly present-day, ongoing) unstable retreat of the West Antarctic ice sheet (e.g., Joughin et al., 2014; Hulbe, 2017; Konrad et al., 2018). Because a loss of ice shelf buttressing is a primary cause of increased GLF (and thus an indirect control on the MISI), recent attention has focused on better understanding the sensitivity of ice shelf buttressing to increases in iceberg calving and sub-ice shelf melting. In this study, we have attempted to better characterize and quantify how local thickness perturbations on ice shelves – a proxy for local thinning due to increased sub-ice shelf melting – impact ice shelf buttressing and GLF.

Two previous approaches for assessing GLF sensitivity to changes in ice shelf buttressing – the flux response number (N_{rp}) and the buttressing number (N_b) – show significant correlations with one another only over regions with a relatively small shear component. In addition, this correlation is highly dependent on the direction chosen to define buttressing. Specifically, we find that the choice of the normal vector used when calculating N_b dictates whether the correlation between N_{rp} and N_b is significant or not. Here, for both idealized and realistic ice shelf domains, we find a weak correlation between N_{rp} and N_b when the normal stress used in calculating the buttressing number corresponds to the second principal stress direction (\mathbf{n}_{p2}). The correlation is stronger (though sometimes still fairly weak) when N_b is calculated in the direction associated with the first principal stress (\mathbf{n}_{p1}) or the ice flow (\mathbf{n}_f).

These findings appear at odds with the interpretation from previous efforts of Fürst et al. (2016), who argue that buttressing provided by an ice shelf is best quantified by N_b calculated in the direction of \mathbf{n}_{p2} . The seeming contradiction may be partially rectified by considering the different foci of Fürst et al. (2016) versus the present work: while Fürst et al. (2016) primarily focused on how the removal of passive shelf ice (identified by $N_b(\mathbf{n}_{p2})$) impacted ice shelf dynamics, as quantified by the *change in ice flux across the calving front*, our focus is specifically on how localized ice shelf thickness perturbations impact the *change in ice flux across the grounding line*¹. While changes in calving flux are likely to impact the amount of buttressing provided by an ice shelf, they do not directly contribute to changes in sea level. For this reason, changes in GLF are arguably the more important metric to consider when assessing the impacts of changes in ice shelf buttressing.

Of significant concern in applying the apparent correlation between N_{rp} and N_b (relatively difficult and easy quantities to calculate, respectively) is the lack of a clear physical connection between local changes in buttressing on the ice shelf and integrated changes in flux at the grounding line. Here, we show that localized thinning on the shelf can lead to either increases or decreases in the local buttressing metric N_b , depending on both the direction of the normal stress chosen and the neighborhood over which these changes are estimated. Yet these same perturbations consistently result in a net *decrease* in buttressing and consequently a net *increase* in grounding line flux. While this can often be understood through the detailed spatial analysis of the impacts for a single perturbation (e.g., Section 4.3 and Fig.6), this finding suggests that local evaluations of buttressing on the ice shelf alone should be interpreted with extreme caution, as they may not be physically meaningful with respect to

¹While Fürst et al. (2016) also discuss the impact of perturbations on the flux across the grounding line, this is a secondary focus of their paper and mostly discussed in the Supplementary Material.

understanding overall changes in GLF. It is also possible that the correlations we find between N_{rp} and N_b are fortuitous or spurious, giving us further pause in attempting to apply them in a predictive sense.

Practically speaking, however, these nuances may be irrelevant; when realistic and complex ice shelf geometries are considered, clear and robust relationships between N_{rp} and N_b are elusive or absent. For the Larsen C domain considered here, 385 strong, positive correlations are only found to exist over a small, isolated region near the center of the ice shelf; proximity to the grounding line, the calving front, complex coastlines, islands, and promontories all serve to degrade these correlations significantly, reducing the utility of the buttressing number as a simple metric for diagnosing GLF sensitivity on real ice shelves. Further, defining “proximity”, and hence an adequate distance away from these complicating features or other filtering metric, appears to be largely arbitrary. Lastly, it is precisely these more complex regions, close to the ice shelf grounding lines, where 390 sub-ice shelf thinning will result in the largest impact on changes in GLF (as demonstrated in Figs. 11a and 12a).

Considering these complexities, we propose that assessing GLF sensitivities for real ice shelves requires an approach analogous to the perturbation method used by Reese et al. (2018). Due to the computational costs and the experimental design complexity associated with the perturbation-based method we propose that an adjoint-based method is the more efficient way for assessing GLF sensitivity to changes in buttressing resulting from changes in sub-ice shelf melting. Future work should 395 focus on applying these methods to assessing the sensitivities of real ice shelves, based on observed or modeled patterns of sub-ice shelf melting, and assessing how these sensitivities change in time along with the evolution of the coupled ocean-and-ice shelf system.

6 Acknowledgements

The authors thank Hilmar Gudmundsson, two anonymous reviewers, and the editor, Olivier Gagliardini, for comments and suggestions that significantly improved the manuscript. Support for this work was provided through the Scientific Discovery 400 through Advanced Computing (SciDAC) program funded by the U.S. Department of Energy (DOE) Office of Science, Biological and Environmental Research and Advanced Scientific Computing Research programs. This research used resources of the National Energy Research Scientific Computing Center, a DOE Office of Science user facility supported by the Office of Science of the U.S. Department of Energy under Contract DE-AC02-05CH11231, and resources provided by the Los Alamos 405 National Laboratory Institutional Computing Program, which is supported by the U.S. Department of Energy National Nuclear Security Administration under Contract DE-AC52-06NA25396.

7 Code and data availability

The code of the ice sheet model (MALI) can be found here: <https://github.com/MPAS-Dev/MPAS-Model/releases> (V6.0). The datasets used in this paper can be found in <https://doi.org/10.5281/zenodo.3872586>.

410 8 Author contribution

Tong Zhang and Stephen Price initiated the study with input from Matthew Hoffman, Mauro Perego, and Xylar Asay-Davis. Tong Zhang conducted the diagnostic simulations with MALI and the majority of the analysis. The adjoint experiments were conducted by Mauro Perego. All authors contributed to the writing of the paper.

9 Competing interests

415 The authors declare that they have no conflict of interest.

Appendix A: Calculation of the buttressing number

At the calving front, the stress balance is given by,

$$\sigma \cdot \mathbf{n} = -p_w \mathbf{n}, \quad (\text{A1})$$

where σ is the Cauchy stress tensor, \mathbf{n} is the unit normal vector pointing horizontally away from the calving front, and p_w is the water pressure against the calving front provide by the ocean. In a Cartesian reference frame, this gives two equations for the stress balance in the two horizontal directions,

$$\sigma_{xx}n_x + \sigma_{xy}n_y = -p_w n_x, \quad (\text{A2})$$

$$\sigma_{xy}n_x + \sigma_{yy}n_y = -p_w n_y.$$

Expressing the Cauchy stress as the sum of the deviatoric stress and the isotropic pressure ($\sigma = \tau - pI$) and assuming that the vertical normal stress σ_{zz} is hydrostatic gives,

$$425 \quad p = \rho_i g(s - z) - \tau_{xx} - \tau_{yy}. \quad (\text{A3})$$

Combining Equations A2 and A3 gives,

$$(2\tau_{xx} + \tau_{yy})n_x + \tau_{xy}n_y = -p_w n_x + \rho_i g(s - z)n_x, \quad (\text{A4})$$

$$\tau_{xy}n_x + (2\tau_{yy} + \tau_{xx})n_y = -p_w n_y + \rho_i g(s - z)n_y.$$

On ice shelves, the left hand terms in Equations A4 can be taken as invariant in the z direction and by vertically averaging A4 we obtain

$$430 \quad (2\tau_{xx} + \tau_{yy})n_x + \tau_{xy}n_y = \frac{1}{2}\rho_i g\left(1 - \frac{\rho}{\rho_w}\right)Hn_x, \quad (\text{A5})$$

$$\tau_{xy}n_x + (2\tau_{yy} + \tau_{xx})n_y = \frac{1}{2}\rho_i g\left(1 - \frac{\rho}{\rho_w}\right)Hn_y.$$

If we define the two-dimensional stress tensor \mathbf{T} as,

$$\mathbf{T} = \begin{pmatrix} 2\tau_{xx} + \tau_{yy} & \tau_{xy} \\ \tau_{xy} & 2\tau_{yy} + \tau_{xx} \end{pmatrix}, \quad (\text{A6})$$

we can write Eq. (A5) as

$$\mathbf{Tn} = N_0 \mathbf{n}, \quad (\text{A7})$$

435 where $N_0 = \frac{1}{2} \rho_i g (1 - \rho_i / \rho_w) H$ is the average pressure exerted by the ocean against the calving front (as defined in Eq. (11)).
The buttressing number, defined by

$$N_b = 1 - \frac{\mathbf{n} \cdot \mathbf{Tn}}{N_0}, \quad (\text{A8})$$

is thus a scalar measure of the balance between this average ocean pressure and internal stress within the ice shelf. For the case of $N_b = 0$, these two exactly balance such that stresses within the ice shelf do not further restrain or compel the ice flow.

440 **Appendix B: Relationship between buttressing number and backstress**

Thomas (1979) defines the concept of “back-pressure” or “back stress”, which was formalized by Thomas and MacAyeal (1982) and MacAyeal (1987) as the stress provided by lateral shearing and compression around ice rises in excess of that of a freely spreading ice shelf. While the concept was conceived as applying along the grounding line (Thomas, 1979; MacAyeal, 1987), it was extended to any material surface within an ice shelf (Thomas and MacAyeal, 1982; MacAyeal, 1987). This older
445 concept of a normal pressure characterizing downstream ice shelf conditions is reminiscent of the buttressing number defined by Gudmundsson (2013) and extended by Fürst et al. (2016) as the buttressing number (N_b), defined in Eq. (A8) (and Eq. (10)). Here we show that backstress is equivalent to N_b calculated in the along flow direction and normalized by the hydrostatic stress.

We follow Van Der Veen (2013) and Cuffey and Paterson (2010) and define back force, F_B , as the difference between the driving force of an ice shelf, F_D and the resistive force from longitudinal stretching, F_L :

$$450 \quad F_B = F_D - F_L. \quad (\text{B1})$$

The driving force for an ice shelf is

$$F_D = \frac{1}{2} \rho_i g \left(1 - \frac{\rho_i}{\rho_w}\right) H^2, \quad (\text{B2})$$

and the longitudinal stretching force for a freely spreading ice shelf is

$$F_L = H(2\tau_{xx}^f + \tau_{yy}^f), \quad (\text{B3})$$

455 where τ_{xx}^f and τ_{yy}^f are the along-flow and across-flow deviatoric stresses, respectively. Therefore,

$$F_L = HT_{xx}^f, \quad (\text{B4})$$

according to Eq. (A6), where T_{xx}^f is the along-flow stress in the along-flow coordinate system, equivalent to the normal stress along the flow direction, $\mathbf{n}_f \cdot \mathbf{Tn}_f$, in the x, y coordinate system. To obtain the backstress, B_s , as a stress normal to a vertically-oriented material surface, divide Eq. (B1) by thickness (force per unit width divided by thickness):

$$460 \quad B_s = \frac{F_B}{H} = \frac{F_D}{H} - \frac{F_L}{H}. \quad (\text{B5})$$

However, if we observe that the driving stress of an ice shelf is the hydrostatic stress, N_0 (Eq. (11)), multiplied by the thickness,

$$F_D = N_0 H, \quad (\text{B6})$$

combined with Eq. (B4), we can rewrite the backstress as

$$465 \quad B_s = N_0 - \mathbf{n}_f \cdot \mathbf{T} \mathbf{n}_f. \quad (\text{B7})$$

Dividing (normalizing) by N_0 then gives

$$\frac{B_s}{N_0} = 1 - \frac{\mathbf{n}_f \cdot \mathbf{T} \mathbf{n}_f}{N_0} = N_b(\mathbf{n}_f), \quad (\text{B8})$$

which is analogous to Eq. (A8) above.

This result, while fairly straightforward to arrive at, brings together the current concept of “buttressing” at the grounding
470 line (as defined by Gudmundsson (2013) and extended to “buttressing number” on the ice shelf by Fürst et al. (2016)), with the much older concept of ice shelf “backstress” (e.g., Thomas and MacAyeal, 1982).

Appendix C: Adjoint calculation of GLF sensitivity

The adjoint method is often used to compute the derivative (or “sensitivity”) of some quantity (here, the GLF) that depends on the solution of a partial differential equation, with respect to parameters (here, the ice thickness) (see, e.g., Gunzburger (2012)).
475 It is particularly effective when the number of parameters is large because it only requires the solution of an additional linear system, independent of the number of parameters. In the discrete case, the GLF is a function of the ice speed vector, \mathbf{u} , and the ice thickness vector, \mathbf{H} . Using the chain rule, we compute the total derivative of the GLF with respect to the ice thickness as:

$$\frac{d(\text{GLF})}{d\mathbf{H}} = \frac{\partial(\text{GLF})}{\partial \mathbf{u}} \frac{\partial \mathbf{u}}{\partial \mathbf{H}} + \frac{\partial(\text{GLF})}{\partial \mathbf{H}}. \quad (\text{C1})$$

Here $\frac{\partial \mathbf{u}}{\partial \mathbf{H}}$ denotes the matrix with components $\left(\frac{\partial \mathbf{u}}{\partial \mathbf{H}} \right)_{ij} = \frac{\partial u_i}{\partial H_j}$. Similarly $\frac{\partial(\text{GLF})}{\partial \mathbf{u}}$ and $\frac{\partial(\text{GLF})}{\partial \mathbf{H}}$ are row vectors with com-
480 ponents $\frac{\partial(\text{GLF})}{\partial u_j}$ and $\frac{\partial(\text{GLF})}{\partial H_j}$ respectively. The first term on the right-hand side of Eq. (C1) accounts for the fact that a perturbation of the thickness would affect the ice velocity, which in turn would affect the GLF. The second term on the right-hand side of Eq. (C1) accounts for changes in the GLF directly due to changes in thickness and is non-zero only when the thickness is perturbed at triangles intersecting the GL. In this case, a thickness perturbation would affect the position/length of the GL and the thickness of the ice at the GL.

485 In order to compute $\frac{\partial \mathbf{u}}{\partial \mathbf{H}}$, we write the finite element discretization (Tezaur et al. (2015b)) of the flow model (Eq. (1)) in the residual form $\mathbf{c}(\mathbf{u}, \mathbf{H}) = \mathbf{0}$ and differentiate with respect to \mathbf{H} :

$$\mathbf{0} = \frac{d\mathbf{c}}{d\mathbf{H}} = \frac{\partial \mathbf{c}}{\partial \mathbf{u}} \frac{\partial \mathbf{u}}{\partial \mathbf{H}} + \frac{\partial \mathbf{c}}{\partial \mathbf{H}}. \quad (\text{C2})$$

Here $J := \frac{\partial \mathbf{c}}{\partial \mathbf{u}}$ is a square matrix referred to as the Jacobian. It follows that $\frac{\partial \mathbf{u}}{\partial \mathbf{H}}$ is solution of

$$J \frac{\partial \mathbf{u}}{\partial \mathbf{H}} = -\frac{\partial \mathbf{c}}{\partial \mathbf{H}}. \quad (\text{C3})$$

490 Note that this corresponds to solving many linear systems, one for each column of $\frac{\partial \mathbf{u}}{\partial \mathbf{H}}$ (i.e. for each entry of the ice thickness vector). We can then compute the sensitivity as

$$\frac{d(\text{GLF})}{d\mathbf{H}} = -\frac{\partial(\text{GLF})}{\partial \mathbf{u}} \left(J^{-1} \frac{\partial \mathbf{c}}{\partial \mathbf{H}} \right) + \frac{\partial(\text{GLF})}{\partial \mathbf{H}}. \quad (\text{C4})$$

The main idea of the adjoint-based method is to introduce an auxiliary vector variable $\boldsymbol{\lambda}$ for solution of the *adjoint* system

$$J^T \boldsymbol{\lambda} = -\left(\frac{\partial(\text{GLF})}{\partial \mathbf{u}} \right)^T \quad (\text{C5})$$

495 and then to compute the sensitivity as

$$\frac{d(\text{GLF})}{d\mathbf{H}} = \boldsymbol{\lambda}^T \frac{\partial \mathbf{c}}{\partial \mathbf{H}} + \frac{\partial(\text{GLF})}{\partial \mathbf{H}}. \quad (\text{C6})$$

Equations (C4) and (C6) are equivalent, but the latter has the advantage of requiring the solution of a single linear system given by Equation (C5). In MALI, the Jacobian and the other derivatives, $\frac{\partial \mathbf{c}}{\partial \mathbf{H}}$, $\frac{\partial(\text{GLF})}{\partial \mathbf{u}}$, and $\frac{\partial(\text{GLF})}{\partial \mathbf{H}}$, are computed using automatic differentiation, a technique that allows for exact calculation of derivatives up to machine precision. For automatic-
500 differentiation, MALI relies on the Trilinos *Sacado* package (Phipps and Pawlowski, 2012). As a final remark, we note that the term $\frac{\partial \mathbf{c}}{\partial \mathbf{H}}$ requires the computation of shape derivatives, because a change in thickness affects the geometry of the problem. This is not the case for two-dimensional, depth-integrated flow models (e.g., as in Goldberg et al. (2019)), or when using a sigma-coordinate to discretize the vertical dimension.

We conclude this section pointing out that the sensitivity $\frac{d(\text{GLF})}{d\mathbf{H}}$ depends on the local refinement of the mesh and it
505 vanishes as the mesh is refined. This is particularly important in the case of nonuniform meshes, because the sensitivity map would strongly depend on the refinement. In order to overcome this issue it is advisable to scale the sensitivity pre-multiplying it by the inverse of the mass matrix (in a finite element context) or, similarly, dividing it point-wise by the measure (area) of the dual cells, as done in this paper to compute N_{ra} . We refer to Li et al. (2017), Section 6, for an in-depth analysis, in the optimization context.

510 **References**

- Asay-Davis, X. S., Cornford, S. L., Durand, G., Galton-Fenzi, B. K., Gladstone, R. M., Gudmundsson, H., Hattermann, T., Holland, D. M., Holland, D., Holland, P. R., et al.: Experimental design for three interrelated marine ice sheet and ocean model intercomparison projects: MISMIP v. 3 (MISMIP+), ISOMIP v. 2 (ISOMIP+) and MISOMIP v. 1 (MISOMIP1), *Geoscientific Model Development*, 9, 2471–2497, 2016.
- 515 Bamber, J. L., Riva, R. E., Vermeersen, B. L., and Lebrocq, A. M.: Reassessment of the potential sea-level rise from a collapse of the west antarctic ice sheet, *Science*, 324, 901–903, <https://doi.org/10.1126/science.1169335>, www.sciencemag.org/cgi/content/full/324/5929/901, 2009.
- Brondeux, J., Gagliardini, O., Gillet-Chaulet, F., and Durand, G.: Sensitivity of grounding line dynamics to the choice of the friction law, *Journal of Glaciology*, 63, 854–866, 2017.
- 520 Cornford, S., Seroussi, H., Asay-Davis, X., Arthern, R., Borstad, C., Christmann, J., Dias dos Santos, T., Feldmann, J., Goldberg, D., Hoffman, M., Humbert, A., Kleiner, T., Leguy, G., Lipscomb, W., Merino, N., Durand, G., Morlighem, M., Pollard, D., Rückamp, M., and Yu, H.: Results of the third Marine Ice Sheet Model Intercomparison Project (MISMIP+), *The Cryosphere*, 14, 2283–2301, <https://doi.org/10.5194/tc-14-2283-2020>, 2020.
- Cornford, S. L., Martin, D. F., Payne, A. J., Ng, E. G., Le Brocq, A. M., Gladstone, R. M., Edwards, T. L., Shannon, S. R., Agosta, C., van den
525 Broeke, M. R., Hellmer, H. H., Krinner, G., Ligtenberg, S. R. M., Timmermann, R., and Vaughan, D. G.: Century-scale simulations of the response of the West Antarctic Ice Sheet to a warming climate, *The Cryosphere*, 9, 1579–1600, <https://doi.org/10.5194/tc-9-1579-2015>, 2015.
- Cuffey, K. and Paterson: *The Physics of Glaciers*, Butterworth-Heinemann, Amsterdam, 4th edn., 2010.
- De Rydt, J., Gudmundsson, G., Rott, H., and Bamber, J.: Modeling the instantaneous response of glaciers after the collapse of the Larsen B
530 Ice Shelf, *Geophysical Research Letters*, 42, 5355–5363, 2015.
- Fretwell, P., Pritchard, H. D., Vaughan, D. G., Bamber, J., Barrand, N., Bell, R., Bianchi, C., Bingham, R., Blankenship, D., Casassa, G., et al.: Bedmap2: improved ice bed, surface and thickness datasets for Antarctica, *The Cryosphere*, 7, 375–393, <https://doi.org/10.5194/tc-7-375-2013>, 2013.
- Fürst, J. J., Durand, G., Gillet-Chaulet, F., Tavard, L., Rankl, M., Braun, M., and Gagliardini, O.: The safety band of Antarctic ice shelves,
535 *Nature Climate Change*, 6, 479, 2016.
- Gagliardini, O., Durand, G., Zwinger, T., Hindmarsh, R., and Le Meur, E.: Coupling of ice-shelf melting and buttressing is a key process in ice-sheets dynamics, *Geophysical Research Letters*, 37, 2010.
- Goldberg, D. N., Gourmelen, N., Kimura, S., Millan, R., and Snow, K.: How Accurately Should We Model Ice Shelf Melt Rates?, *Geophysical Research Letters*, 46, 189–199, <https://doi.org/10.1029/2018GL080383>, 2019.
- 540 Gudmundsson, G.: Ice-shelf buttressing and the stability of marine ice sheets, *The Cryosphere*, 7, 647–655, 2013.
- Gudmundsson, H., Krug, J., Durand, G., Favier, L., and Gagliardini, O.: The stability of grounding lines on retrograde slopes, *The Cryosphere*, 6, 1497–1505, 2012.
- Gunzburger, M. D.: *Perspectives in Flow Control and Optimization: Chapter 2. Three Approaches to Optimal Control and Optimization*, Siam, <https://doi.org/10.1137/1.9780898718720.ch2>, 2012.
- 545 Haseloff, M. and Sergienko, O. V.: The effect of buttressing on grounding line dynamics, *Journal of Glaciology*, 64, 417–431, 2018.

- Hoffman, M. J., Perego, M., Price, S. F., Lipscomb, W. H., Zhang, T., Jacobsen, D., Tezaur, I., Salinger, A. G., Tuminaro, R., and Bertagna, L.: MPAS-Albany Land Ice (MALI): a variable-resolution ice sheet model for Earth system modeling using Voronoi grids, *Geoscientific Model Development*, 11, 3747–3780, <https://doi.org/10.5194/gmd-11-3747-2018>, <https://www.geosci-model-dev.net/11/3747/2018/>, 2018.
- 550 Hulbe, C.: Is ice sheet collapse in West Antarctica unstoppable?, *Science*, 356, 910–911, 2017.
- Hutter, K.: *Theoretical glaciology*, Reidel Publ., Dordrecht, Netherlands, <https://doi.org/10.1007/978-94-015-1167-4>, 1983.
- Jenkins, A., Dutrieux, P., Jacobs, S., Steig, E. J., Gudmundsson, G. H., Smith, J., and Heywood, K. J.: Decadal ocean forcing and Antarctic ice sheet response: Lessons from the Amundsen Sea, *Oceanography*, 29, 106–117, 2016.
- Joughin, I., Smith, B. E., and Medley, B.: Marine ice sheet collapse potentially under way for the Thwaites Glacier Basin, West Antarctica, 555 *Science*, 344, 735–738, 2014.
- Konrad, H., Shepherd, A., Gilbert, L., Hogg, A. E., McMillan, M., Muir, A., and Slater, T.: Net retreat of Antarctic glacier grounding lines, *Nature Geoscience*, 11, 258, 2018.
- Li, D., Gurnis, M., and Stadler, G.: Towards adjoint-based inversion of time-dependent mantle convection with nonlinear viscosity, *Geophysical Journal International*, 209, 86–105, <https://doi.org/10.1093/gji/ggw493>, <https://doi.org/10.1093/gji/ggw493>, 2017.
- 560 Liefvering, B. V. and Pattyn, F.: Using ice-flow models to evaluate potential sites of million year-old ice in Antarctica, *Climate of the Past*, 9, 2335–2345, 2013.
- MacAyeal, D. R.: Ice-shelf backpressure: form drag versus dynamic drag, in: *Dynamics of the West Antarctic Ice Sheet*, edited by Van Der Veen, C. J. and Oerlemans, J., p. 141, D. Reidel Publishing Company, Dordrecht, Holland, 1987.
- Mercer, J. H.: West Antarctic ice sheet and CO₂ greenhouse effect: a threat of disaster, *Nature*, 271, 321, 1978.
- 565 Morland, L.: Unconfined ice-shelf flow, in: *Dynamics of the West Antarctic Ice Sheet*, pp. 99–116, Springer, 1987.
- Pegler, S. S.: Marine ice sheet dynamics: the impacts of ice-shelf buttressing, *Journal of Fluid Mechanics*, 857, 605–647, 2018a.
- Pegler, S. S.: Suppression of marine ice sheet instability, *Journal of Fluid Mechanics*, 857, 648–680, 2018b.
- Pegler, S. S. and Worster, M. G.: Dynamics of a viscous layer flowing radially over an inviscid ocean, *Journal of Fluid Mechanics*, 696, 152–174, 2012.
- 570 Perego, M., Gunzburger, M., and Burkardt, J.: Parallel finite-element implementation for higher-order ice-sheet models, *Journal of Glaciology*, 58, 76–88, <https://doi.org/10.3189/2012JoG11J063>, 2012.
- Perego, M., Price, S., and Stadler, G.: Optimal initial conditions for coupling ice sheet models to Earth system models, *Journal of Geophysical Research: Earth Surface*, 119, 1894–1917, 2014.
- Phipps, E. and Pawlowski, R.: Efficient Expression Templates for Operator Overloading-Based Automatic Differentiation, in: *Recent Advances in Algorithmic Differentiation*, edited by Forth, S., Hovland, P., Phipps, E., Utke, J., and Walther, A., vol. 87 of *Lecture Notes in Computational Science and Engineering*, pp. 309–319, Springer, Berlin, https://doi.org/10.1007/978-3-642-30023-3_28, 2012.
- 575 Reese, R., Gudmundsson, G. H., Levermann, A., and Winkelmann, R.: The far reach of ice-shelf thinning in Antarctica, *Nature Climate Change*, 8, 53, 2018.
- Rignot, E., Mouginot, J., and Scheuchl, B.: Ice flow of the antarctic ice sheet, *Science*, 333, 1427–1430, 580 <https://doi.org/10.1126/science.1208336>, 2011.
- Rignot, E., Mouginot, J., Morlighem, M., Seroussi, H., and Scheuchl, B.: Widespread, rapid grounding line retreat of Pine Island, Thwaites, Smith, and Kohler glaciers, West Antarctica, from 1992 to 2011, *Geophysical Research Letters*, 41, 3502–3509, 2014.

- Royston, S. and Gudmundsson, G. H.: Changes in ice-shelf buttressing following the collapse of Larsen A Ice Shelf, Antarctica, and the resulting impact on tributaries, *Journal of Glaciology*, 62, 905–911, 2016.
- 585 Schoof, C.: Ice sheet grounding line dynamics: Steady states, stability, and hysteresis, *Journal of Geophysical Research: Earth Surface*, 112, 2007.
- Seroussi, H., Morlighem, M., Larour, E., Rignot, E., and Khazendar, A.: Hydrostatic grounding line parameterization in ice sheet models, *The Cryosphere*, 8, 2075–2087, 2014.
- Seroussi, H., Nowicki, S., Simon, E., Abe-Ouchi, A., Albrecht, T., Brondex, J., Cornford, S., Dumas, C., Gillet-Chaulet, F., Goelzer, H.,
590 Gollledge, N. R., Gregory, J. M., Greve, R., Hoffman, M. J., Humbert, A., Huybrechts, P., Kleiner, T., Larour, E., Leguy, G., Lipscomb, W. H., Lowry, D., Mengel, M., Morlighem, M., Pattyn, F., Payne, A. J., Pollard, D., Price, S. F., Quiquet, A., Reerink, T. J., Reese, R., Rodehacke, C. B., Schlegel, N.-J., Shepherd, A., Sun, S., Sutter, J., Van Breedam, J., van de Wal, R. S. W., Winkelmann, R., and Zhang, T.: initMIP-Antarctica: an ice sheet model initialization experiment of ISMIP6, *The Cryosphere*, 13, 1441–1471, <https://doi.org/10.5194/tc-13-1441-2019>, <https://www.the-cryosphere.net/13/1441/2019/>, 2019.
- 595 Tezaur, I. K., Perego, M., Salinger, A. G., Tuminaro, R. S., and Price, S.: Albany/FELIX: a parallel, scalable and robust, finite element, first-order Stokes approximation ice sheet solver built for advanced analysis, *Geoscientific Model Development*, 8, 1–24, <https://doi.org/10.5194/gmd-8-1-2015>, 2015a.
- Tezaur, I. K., Tuminaro, R. S., Perego, M., Salinger, A. G., and Price, S. F.: On the scalability of the Albany/FELIX first-order Stokes approximation ice sheet solver for large-scale simulations of the Greenland and Antarctic ice sheets, *Procedia Computer Science*, 51,
600 2026–2035, 2015b.
- Thomas, R. H.: The dynamics of marine ice sheets, *The Journal of Glaciology*, 24, 167–178, 1979.
- Thomas, R. H. and MacAyeal, D. R.: Derived Characteristics of the Ross Ice Shelf, Antarctica, *Journal of Glaciology*, 28, 397–412, <https://doi.org/10.3189/s0022143000005025>, 1982.
- Van Der Veen, C. J.: *Fundamentals of Glacier Dynamics*, CRC Press, Boca Raton, FL, 2 edn., 2013.
- 605 Wearing, M.: *The Flow Dynamics and Buttressing of Ice Shelves*, Ph.D. thesis, University of Cambridge, 2016.